Image-domain and data-domain waveform tomography: a case study

Esteban Díaz[1], *Yuting Duan*[1], *Gerhard Pratt*[2], *and Paul Sava*[1]
[1] *Center for Wave Phenomena, Colorado School of Mines,* [2] *University of Western Ontario*

SUMMARY

Wavefield-based tomographic methods are idoneous for recovering velocity models from seismic data. The use of wavefields rather than rays is more consistent with the bandlimited nature of seismic data. Image domain methods seek to improve the focusing in extended images, thus producing better seismic images. However, image domain methods produce low resolution models due to the fact that their objective functions are smooth, particularly in the vicinity of the global minimum. In contrast, data-domain methods produce high resolution models but suffer from strong non-linearity causing cycle skipping if certain conditions are not met. By combining the characteristics of each method, we can obtain models that produce better images and contain high resolution features at the same time. We demonstrate a the workflow that combines both methods with an application to a broadband marine 2D dataset with a variable streamer depth.

INTRODUCTION

Velocity analysis methods based on wavefield extrapolation are commonly referred to as Wavefield Tomography (WT) (Tarantola, 1984; Woodward, 1992; Pratt, 1999; Sava and Biondi, 2004a,b; Shen and Symes, 2008; Biondi and Symes, 2004; Symes, 2008); such tomographic approaches can be formulated either in the image domain, where one tries to improve image quality, or in the data domain, where one seeks consistency between modeled and observed data.

Image-domain wavefield tomography (iWT) can be formulated by many means. A common approach aims to improve the flatness of angle gathers; equivalently one can improve the focusing of space-lag gathers (Shen and Calandra, 2005). Space-lag gathers (Rickett and Sava, 2002; Sava and Fomel, 2006) measure the spatial similarity between source and receiver wavefields. Hence, during tomography, one seeks to increase the similarity of the spatial correlation for a collection of seismic experiments (Shen and Symes, 2008; Yang and Sava, 2011; Weibull and Arntsen, 2013; Yang et al., 2013; Shan and Wang, 2013). Inverse problems formulated in the image domain are generally better-posed than those formulated in the data domain.

Data-domain wavefield tomography (dWT) is generally formulated by improving the consistency between modeled and observed data. Originally, Tarantola (1984) introduced the data difference as a similarity estimate in the time domain. Alternatively, the problem can be posed in the frequency domain (Pratt and Worthington, 1990; Pratt et al., 1998). In contrast to the image-domain formulation, data-domain wavefield tomography is highly non-linear resulting in an objective function with many local minima. To overcome the non-linearity, a multi-scale separation approach is needed (Bunks et al., 1995; Brenders and Pratt, 2007). Within each scale (wavenumber band or frequency band), the problem can be more linear if the initial model is closer to the one corresponding to the global minimum. Another loop of multi-scale can be added by introducing time damping, a method commonly referred to as Laplace-Fourier waveform inversion (Sirgue and Pratt, 2004; Shin and Ho Cha, 2009). The purpose of the time damping is to fit earlier arrivals first, and then to fit later arrivals progressively.

Both data-domain and image-domain tomographic methods share many parts of the process: both use the same extrapolation engine (the two-way wave equation), and share similarities in building the gradient of the objective function through the Adjoint State framework (Tarantola, 1984; Plessix, 2006; Symes, 2008).

Both tomographic methods are complementary. Therefore, in this abstract, we combine image-domain and data-domain wavefield tomography approaches for optimizing the velocity model. The idea is to produce a model that improves focusing with image-domain wavefield tomography and then refine it using data-domain wavefield tomography. We apply the cascaded workflow to a marine 2D dataset. The data are acquired with a variable depth streamer cable, which produces a diverse notch spectrum (Soubaras and Dowle, 2010). The increased depth produces a better low frequency response, which can be useful in the multi-scale approach discussed earlier.

IMAGE-DOMAIN WT

Space-lag gathers (Rickett and Sava, 2002; Sava and Vasconcelos, 2011) highlight the spatial consistency between wavefields by exploring the focusing information in the image domain. The focusing in the gather is sensitive to velocity perturbations, and hence can be optimized. Space-lag gathers are defined as follows:

$$R(\mathbf{x},\boldsymbol{\lambda}) = \sum_{e,t} u_s(e,\mathbf{x}-\boldsymbol{\lambda},t)u_r(e,\mathbf{x}+\boldsymbol{\lambda},t), \qquad (1)$$

where $\boldsymbol{\lambda}$ is the space-lag vector, $\mathbf{x}$ the image location, e the experiment index, u_s the source wavefield, and u_r the receiver wavefield. The source wavefield u_s is produced by forward extrapolation of the source function, whereas the receiver wavefield u_r is produced by backward propagation of the data at the receiver location. In matrix notation, the process is described by

$$\begin{bmatrix} \mathcal{L}(m,t) & 0 \\ 0 & \mathcal{L}^{\top}(m,t) \end{bmatrix} \begin{bmatrix} u_s \\ u_r \end{bmatrix} = \begin{bmatrix} f_s \\ f_r \end{bmatrix}, \qquad (2)$$

where $m = 1/v^2(\mathbf{x})$ is the medium slowness squared, f_s is the source function, f_r is the data at the receiver locations, $\mathcal{L}(m)$, and $\mathcal{L}^\top(m)$ are forward and backward wave propagators, respectively. Here, we use the acoustic wave equation as wave operator:

$$\mathcal{L}(m) = \frac{m(\mathbf{x})}{\rho(\mathbf{x})}\frac{\partial^2}{\partial t^2} - \nabla \cdot \frac{1}{\rho(\mathbf{x})}\nabla. \tag{3}$$

For iWT we use a constant density $\rho(\mathbf{x}) = 1$ km/m^3. A well-focused gather concentrates most of its energy around $\boldsymbol{\lambda} = 0$. This can be used as an optimization criterion by minimizing the energy outside $\boldsymbol{\lambda} = 0$. We can accomplish this by defining an objective function

$$J = \frac{1}{2}\left|\left|P(\boldsymbol{\lambda})R(\mathbf{x},\boldsymbol{\lambda})\right|\right|^2, \tag{4}$$

where $P(\boldsymbol{\lambda})$ is the penalty function, which plays a vital role in the inversion. Depending on the choice of the penalty operator $P(\boldsymbol{\lambda})$, equation 4 can be either minimized or maximized. Here, we use $P(\boldsymbol{\lambda}) = |\boldsymbol{\lambda}|$ (Shen and Symes, 2008) as penalty operator. This penalty operator defines a smooth objective function and corrects for most kinematic errors in the model.

Once we have the penalized gathers (image residuals), we compute the adjoint sources (Shen and Symes, 2008; Weibull and Arntsen, 2013),

$$g_s(\mathbf{x},t) = \sum_{\boldsymbol{\lambda}} P(\boldsymbol{\lambda})^2 R(\mathbf{x}+\boldsymbol{\lambda},\boldsymbol{\lambda})u_r(\mathbf{x}+2\boldsymbol{\lambda},t) \tag{5}$$

for the source terms, and

$$g_r(\mathbf{x},t) = \sum_{\boldsymbol{\lambda}} P(\boldsymbol{\lambda})^2 R(\mathbf{x}-\boldsymbol{\lambda},\boldsymbol{\lambda})u_r(\mathbf{x}-2\boldsymbol{\lambda},t) \tag{6}$$

for the receiver terms. Once we have the adjoint sources, we solve the adjoint equations

$$\begin{bmatrix}\mathcal{L}^\top(m,t) & 0\\ 0 & \mathcal{L}(m,t)\end{bmatrix}\begin{bmatrix}a_s\\ a_r\end{bmatrix} = \begin{bmatrix}g_s\\ g_s\end{bmatrix}, \tag{7}$$

and compute the gradient of equation 4 using

$$\nabla J(\mathbf{x}) = \sum_{e,t}\ddot{u}_s(e,\mathbf{x},t)a_s(e,\mathbf{x},t) + \ddot{u}_r(e,\mathbf{x},t)a_r(e,\mathbf{x},t). \tag{8}$$

DATA-DOMAIN WT

The construction of the tomography problem in the data domain begins with a measure of the error (or residual) at the receiver locations. For dWT, we normally use the data difference

$$J = \frac{1}{2}\left|\left|u_s - f_r\right|\right|^2 = \frac{1}{2}\left|\left|\Delta d^{diff}(e,\mathbf{x}_r,\Omega)\right|\right|^2, \tag{9}$$

or the phase residual

$$J = \frac{1}{2}\left|\left|\arg(u_s) - \arg(f_r)\right|\right|^2 = \frac{1}{2}\left|\left|\Delta d^{phase}(e,\mathbf{x}_r,\Omega)\right|\right|^2, \tag{10}$$

where $\mathbf{x}_r$ are the receiver locations and Ω is the complex valued frequency described below. First, we produce synthetic data by forward propagating the source function $f_s(\mathbf{x}_s,\Omega)$:

$$\mathcal{L}(m,\Omega)u_s = f_s(e,\mathbf{x}_s,\Omega) \tag{11}$$

$\mathcal{L}(m,\Omega)$ is the acoustic wave-equation transformed to the frequency domain. For dWT we parametrize the density $\rho(\mathbf{x})$ as a function of the velocity following Gardner et al. (1974). The adjoint wavefield $a_s(e,\mathbf{x},\Omega)$ is computed by backpropagating the data residual

$$\mathcal{L}^\top(m,\Omega)a_s = \Delta d(e,\mathbf{x}_r,\Omega). \tag{12}$$

Once we obtain $u_s(e,\mathbf{x},\Omega)$ and $a_s(e,\mathbf{x},\Omega)$, we can proceed to compute the gradient:

$$\nabla J(\mathbf{x}) = \mathbb{R}\left\{\sum_{e,t}\Omega^2 u_s(e,\mathbf{x},\Omega)a_s^*(e,\mathbf{x},\Omega)\right\}, \tag{13}$$

here * is the complex conjugate and $\mathbb{R}\{\}$ is the real part. The complex valued frequency $\Omega = \omega + i/\tau$, where τ is the characteristic time for exponential damping, can be used for a multi-scale workflow which can help to circumvent the local minima problems of equation 9 (Sirgue and Pratt, 2004; Shin and Ho Cha, 2009; Kamei et al., 2013). The idea is to first fit lower frequencies ω and earlier arrivals, and then repeat the inversion using longer damping constant τ. In order to get consistent observed data with the damped modeled data, one must also scale the observed data as $f_r(e,\mathbf{x}_r,t) = d_{obs}(e,\mathbf{x}_r,t)e^{-t/\tau}$ before the transformation to frequency domain.

The low frequencies in the data are sensitive to the long wavelength (smooth) components of the earth model. However, if the data do not contain sufficiently low frequencies or sufficiently large offsets, dWT is unable to update such components. In contrast, focusing in extended images is mostly sensitive to the smooth components of the model. By implementing a joint workflow using iWT for updating the smooth components of the model and later using dWT for the high resolution features of the model, we can obtain a more complete spectrum of the model.

APPLICATION TO A REAL 2D DATASET

In this section we demonstrate our proposed workflow with a real 2D marine dataset acquired with a variable depth cable (Soubaras and Dowle, 2010). The streamer contains increased depths as a function of offset, which enhances the frequency content of the data by producing a mixed notch response. Hence, the increasing cable depths improve the low frequency content at intermediate and far offsets which is very helpful for dWT. The acquisition setup in the modeling software mimics the variable depth streamer cable and the free surface, hence it is consistent with the observed data.

We build the initial model, Figure 1(a)(top), by performing time-domain NMO analysis followed by smoothing, RMS (stacking) conversion to interval velocity (Dix,

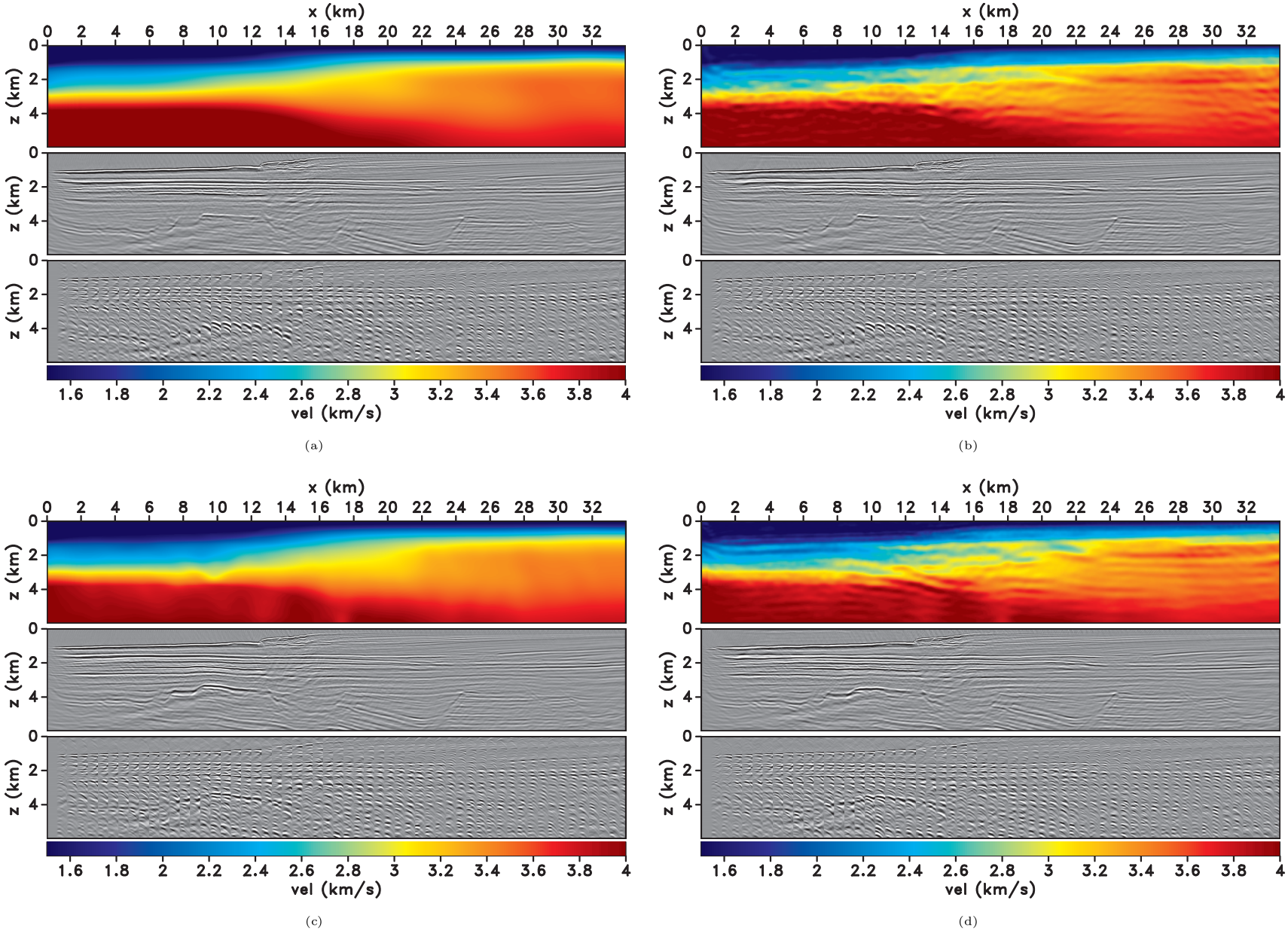

Figure 1: Imaging composition with: velocity (top), RTM image (center) and angle-gathers (bottom) from (a) the initial velocity model, (b) the dWT model built from the starting model, (c) the iWT model, and (d) the dWT model built from the iWT model.

1955), and time to depth conversion. Figure 1(a)(center) shows the corresponding RTM image. One can observe that the image is over-migrated (the velocities are too high) below 3km in depth. Figure 1(a)(bottom) shows angle gathers extracted at sparse locations in the model. Note that we do not use the angle gathers for inversion; instead, we use these particular gathers as an independent quality control tool. The transformation from space-lag gathers $R(\mathbf{x}, \boldsymbol{\lambda})$ to angle domain $R(\mathbf{x}, \theta)$ follows the method of Sava and Fomel (2003). The angles vary from 0 to 45° for all the gathers shown in this abstract. The moveout in the gathers confirms that the velocity is too fast below 3 km. Some of the events in the gathers, however, correspond to migrated multiples and their moveout is not indicative of velocity error.

For dWT, we use 7 successive frequency blocks with 5 simultaneous frequencies each. The center frequency for each block ranges from $f = 2.6$ Hz to $f = 8.9$ Hz. For the time damping constant, we use $\tau = 1.6$ s. We use the phase difference for the data-domain residual. The first step in data domain wavefield tomography involves estimating the source function $f_s(\Omega)$. We use 365 shots for the inversion with a shot interval $\Delta s = 0.09375$ km.

Figure 1(b)(top) shows the dWT model built from Figure 1(a)(top). The dWT process slows the velocity in the shallow part of the section, close to the water bottom, introducing a sharp discontinuity in the model. One can see in the gathers, Figure 1(b)(bottom), that in the shallow part the events get flatter with the new velocity. However, the deeper section does not change significantly. This area of the model corresponds to longer travel-times in the data, and these late arrivals are down-weighted in the inversion by the exponential time damping (in order to avoid cycle skipping).

We generate the model in Figure 1(c)(top) using the iWT approach. The idea of this tomographic step is to correct for the bulk of the kinematic errors in the model. The updated velocity, in general becomes slower, especially in the deep part of the section. Figure 1(c)(center) shows the corresponding RTM image, with increased focusing around $z = 3.5$ km. This observation is confirmed in Figure 1(c)(bottom), where the gathers are flatter throughout the section.

We then update the iWT model using dWT. Figure 1(d)(top) depicts the updated model (compare with Figure 1(b)), which changes considerably in the interval $z = 4$ km to $z = 6$ km. From the corresponding RTM image and angle gathers we can see that the final dWT step does not significantly vary the kinematics of the experiment. However, it introduces subtle structural features in the image. We can see that the structure of the line becomes flatter with the new model (see for instance the event at $z = 4$ km and $x = 18$ to 24 km).

Figures 2(a)-2(d) show the data-domain residuals for the models presented in this section. The residual corresponding to the initial model, Figure 2(a), show large amplitude and phase mismatch. After updating the initial model using dWT, we can see in Figure 2(b) how the residuals improve for intermediate offsets. Figure 2(c) depicts the residual corresponding to the iWT model. We can see that this residuals have smaller energy than those of Figure 2(a). Figure 2(d) shows the residuals for the dWT built from the iWT model. We can see a better match for near and intermediate offsets. The energy for this residual is smaller than any of the previous.

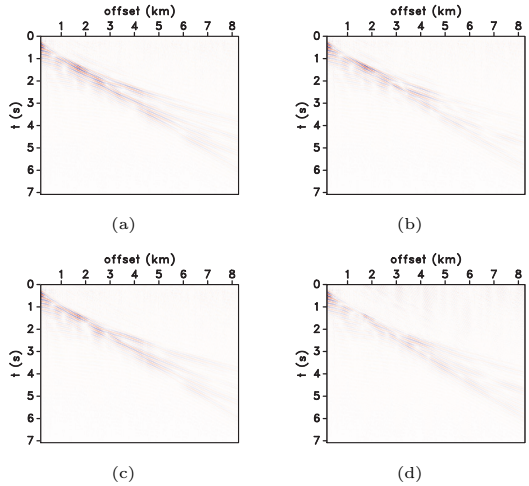

Figure 2: Data domain residuals for shot position $x = 18.75$ km using: (a) the initial velocity model, (b) the dWT model built from the initial model, (c) the iWT model, and (d) the dWT model built from the iWT model.

CONCLUSIONS

The combination of image-domain and data-domain wavefield tomography seeks to exploit the features of each method. Image-domain wavefield tomography methods are sensitive to the smooth components of the model due to the definition of the objective problem. Once we obtain a smooth model that improves focusing in the extended images, we can proceed to further refine the model using data-domain wavefield tomography. We demonstrate the cascaded workflow using a real 2D marine dataset. Our image-domain wavefield tomography model corrects most of the kinematic errors in the model, whereas the data-domain wavefield tomography model corrects early arrival phase errors in the data, and introduces discontinuities in the model directly correlated with events in the image.

ACKNOWLEDGMENTS

We thank sponsor companies of the Consortium Project on Seismic Inverse Methods for Complex Structures. The seismic data shown in this abstract is proprietary to and provided courtesy of CGG. We thank Bruce VerWest for the support with the dataset. The reproducible numeric examples in this paper use the Madagascar open-source software package (Fomel et al., 2013) freely available from http://www.ahay.org.

REFERENCES

Biondi, B., and W. Symes, 2004, Angle-domain common-image gathers for migration velocity analysis by wavefield-continuation imaging: Geophysics, **69**, 1283–1298.

Brenders, A. J., and R. G. Pratt, 2007, Full waveform tomography for lithospheric imaging: results from a blind test in a realistic crustal model: Geophysical Journal International, **168**, 133–151.

Bunks, C., F. Saleck, S. Zaleski, and G. Chavent, 1995, Multiscale seismic waveform inversion: Geophysics, **60**, 1457–1473.

Dix, C., 1955, Seismic velocities from surface measurements: Geophysics, **20**, 68–86.

Fomel, S., P. Sava, I. Vlad, Y. Liu, and V. Bashkardin, 2013, Madagascar: open-source software project for multidimensional data analysis and reproducible computational experiments: Journal of Open Research Software, **1**, e8.

Gardner, G., L. Gardner, and A. Gregory, 1974, Formation velocity and density—the diagnostic basics for stratigraphic traps: Geophysics, **39**, 770–780.

Kamei, R., R. G. Pratt, and T. Tsuji, 2013, On acoustic waveform tomography of wide-angle obs data-strategies for pre-conditioning and inversion: Geophysical Journal International.

Plessix, R.-E., 2006, A review of the adjoint state method for computing the gradient of a functional with geophysical applications: Geophysical Journal International, **167**, 495–503.

Pratt, R., 1999, Seismic waveform inversion in the frequency domain, part 1: Theory and verification in a physical scale model: Geophysics, **64**, 888–901.

Pratt, R. G., C. Shin, and G. J. Hick, 1998, Gauss–newton and full newton methods in frequency–space seismic waveform inversion: Geophysical Journal International, **133**, 341–362.

Pratt, R. G., and M. H. Worthington, 1990, Inverse theory applied to multi-source cross-hole tomography.: Geophysical Prospecting, **38**, 287–310.

Rickett, J. E., and P. C. Sava, 2002, Offset and angle-domain common image-point gathers for shot-profile migration: Geophysics, **67**, 883–889.

Sava, P., and B. Biondi, 2004a, Wave-equation migration velocity analysis - I: Theory: Geophysical Prospecting, **52**, 593–606.

———, 2004b, Wave-equation migration velocity analysis - II: Subsalt imaging examples: Geophysical Prospecting, **52**, 607–623.

Sava, P., and S. Fomel, 2006, Time-shift imaging condition in seismic migration: Geophysics, **71**, S209–S217.

Sava, P., and I. Vasconcelos, 2011, Extended imaging conditions for wave-equation migration: Geophysical Prospecting, **59**, 35–55.

Sava, P. C., and S. Fomel, 2003, Angle-domain common-image gathers by wavefield continuation methods: Geophysics, **68**, 1065–1074.

Shan, G., and Y. Wang, 2013, Rtm based wave equation migration velocity analysis: 4726–4731.

Shen, P., and H. Calandra, 2005, One-way waveform inversion within the framework of adjoint state differential migration: 1709–1712.

Shen, P., and W. W. Symes, 2008, Automatic velocity analysis via shot profile migration: Geophysics, **73**, VE49–VE59.

Shin, C., and Y. Ho Cha, 2009, Waveform inversion in the Laplace–Fourier domain: Geophysical Journal International, **177**, 1067–1079.

Sirgue, L., and R. Pratt, 2004, Efficient waveform inversion and imaging: A strategy for selecting temporal frequencies: Geophysics, **69**, 231–248.

Soubaras, R., and R. Dowle, 2010, Variable-depth streamer–a broadband marine solution: first break, **28**.

Symes, W. W., 2008, Migration velocity analysis and waveform inversion: Geophysical Prospecting, **56**, 765–790.

Tarantola, A., 1984, Inversion of seismic reflection data in the acoustic approximation: Geophysics, **49**, 1259–1266.

Weibull, W., and B. Arntsen, 2013, Automatic velocity analysis with reverse-time migration: Geophysics, **78**, S179–S192.

Woodward, M., 1992, Wave-equation tomography: Geophysics, **57**, 15–26.

Yang, T., and P. Sava, 2011, Image-domain waveform tomography with two-way wave-equation: SEG Technical Program Expanded Abstracts 2011, **508**, 2591–2596.

Yang, T., J. Shragge, and P. Sava, 2013, Illumination compensation for image-domain wavefield tomography: Geophysics, **78**, U65–U76.